

Performance of the restoration of interferometric images from the Large Binocular Telescope – the effects of angular coverage and partial adaptive optics correction

Marcel Carbillet^a, Serge Correia^{b,c}, Patrizia Boccacci^d, Mario Bertero^d

^aINAF – Osservatorio Astrofisico di Arcetri, largo E. Fermi 5, 50125 Firenze, Italy

^bUMR 6525 Astrophysique, UNSA, Parc Valrose, 06108 Nice Cedex 2, France

^cESO, Karl-Schwarzschild-Str. 2, 85748 Garching bei München, Germany

^dINFM and DISI, Università di Genova, via Dodecaneso 33, 16146 Genova, Italy

ABSTRACT

This presentation reports the status of our study concerning the imaging properties of the Large Binocular Telescope (LBT) interferometer, and namely the effect of limited angular coverage and partial adaptive optics (AO) correction. The limitation in angular coverage, together with the correlated problem of angular smearing due to time-averaging of the interferometric images, is investigated for relevant cases depending on the declination of the observed object. Results are encouraging even in case of incomplete coverage. Partial AO-correction can result in a wide range of image quality, but can also create significative differences within a same field-of-view, especially between a suitable reference star to be used for post-observation multiple deconvolution and the observed object. Our study deals with both the problem of space-variance of the AO-corrected point-spread function, and that of global quality of the AO-correction. Uniformity, rather than global quality, is found to be the key-problem. After considering the single-conjugate AO case, we reach to some conclusions for the more interesting, and actually wide-field, case implying multi-conjugate AO. The whole study is performed on different types of object, from binary stars to diffuse objects, and a combined one with a high-dynamic range.

Keywords: Large Binocular Telescope, interferometric imaging, image restoration, adaptive optics

1. INTRODUCTION

The Large Binocular Telescope (LBT) is a Fizeau interferometer made of two 8.4 m pupils placed 14.4 m apart on a common alt-azimuthal mount. It is currently under construction on the top of Mount Graham (Arizona) and first light (with one "eye" of LBT), with its first adaptive optics (AO) system⁹ that includes adaptive secondary mirrors²² and pyramid wavefront sensors, is planned for 2004. Expected performance goes up to $\sim 95\%$ Strehl ratio in the K-band.⁶ In a second step, and for the first-light with both primary mirrors of LBT, an advanced multi-conjugate (MC) AO system will be implemented: NIRVANA/LINC,²¹ permitting high-resolution interferometric imaging on a wide field-of-view. Figure 1 shows the typical LBT interferometric point-spread function (PSF), together with the simulated image of a field of stars within a modelled stellar cluster.⁷

One interesting characteristics of an interferometer such as LBT is the possibility of getting a good coverage of the $u-v$ spatial frequency plane with a few observations at different orientations of the baseline with respect to the sky (i.e. at different parallactic angles). In the case of LBT this is obtained simply thanks to earth rotation which not only produces a rotation of the field (hence the need of a de-rotator), but also a rotation of the projected baseline onto the object. The latter is used to sample the $u-v$ plane. Figure 2 presents a set of PSFs obtained at different (relative) parallactic angles (namely 0° , 60° , and 120°), together with the corresponding optical transfer functions (OTFs), showing the resulting $u-v$ plane coverage.

E-mails: marcel@arcetri.astro.it, scorreia@eso.org, boccacci@disi.unige.it, bertero@disi.unige.it

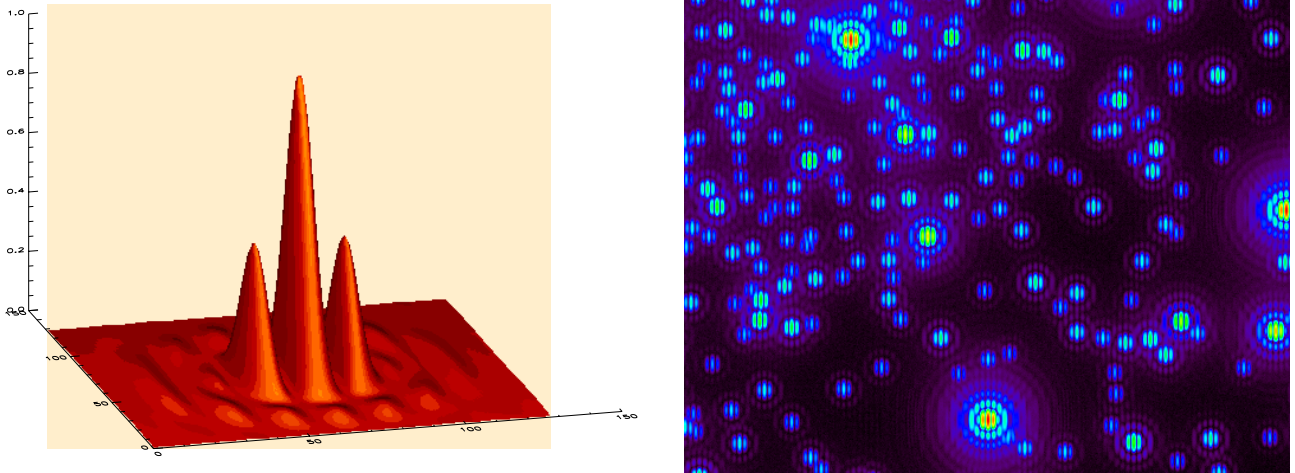


Figure 1. Left: the interferometric PSF of LBT. Right: simulated interferometric LBT image of a part of a star cluster.

The resulting image restoration problem is that a unique high-resolution image of the astronomical object has to be recovered from a set of interferometric observations corresponding to different parallactic angles. Several restoration methods can be applied to this problem.³ In the present study we use the iterative method known as OS-EM (Ordered Subsets - Expectation Maximization), proposed in Bertero & Boccacci,² and implemented within the Software Package AIRY.⁸ It is an accelerated version, when applied to multiple image deconvolution, of the Expectation Maximization (EM) method,¹⁸ also known in astronomy as the Lucy-Richardson method.

The present paper is a direct continuation of a previous published work⁵ which aimed to study the peculiar interferometric imaging performance of LBT by means of numerical simulations, in particular for what concern the limitation in angular coverage and the effect of partial AO-correction. We recall here its main conclusions and report recent developments concerning mainly the partial AO-correction part.

2. THE OS-EM METHOD

Let us assume the image formation to follow $\mathbf{g}_j = \mathbf{K}_j * \mathbf{f} + \mathbf{b}_j + \mathbf{w}_j$, where $*$ stands for convolution, \mathbf{f} is the astronomical object, \mathbf{g}_j ($j = 1, 2, \dots, p$) are the p observations of the object (performed for p different parallactic angles), \mathbf{K}_j are the PSFs related to these observations, \mathbf{b}_j are the average sky backgrounds, and \mathbf{w}_j are the noise terms (additive and not). The image restoration problem is then to estimate \mathbf{f} from the p observations \mathbf{g}_j . Let us also denote by $\mathbf{K}_j^{(-)}$ the PSF obtained by reflecting \mathbf{K}_j with respect to the center of the array. The OS-EM method is as follows:

1. initialize with $\mathbf{f}^{(0)}$ positive (for instance a uniform image);
2. given $\mathbf{f}^{(k)}$ set $\mathbf{h}^{(0)} = \mathbf{f}^{(k)}$ and, for $j = 1, 2, \dots, p$, compute

$$\mathbf{h}^{(j)} = \mathbf{h}^{(j-1)} \mathbf{K}_j^{(-)} * \frac{\mathbf{g}_j}{\mathbf{K}_j * \mathbf{h}^{(j-1)} + \mathbf{b}_j};$$

3. set $\mathbf{f}^{(k+1)} = \mathbf{h}^{(p)}$.

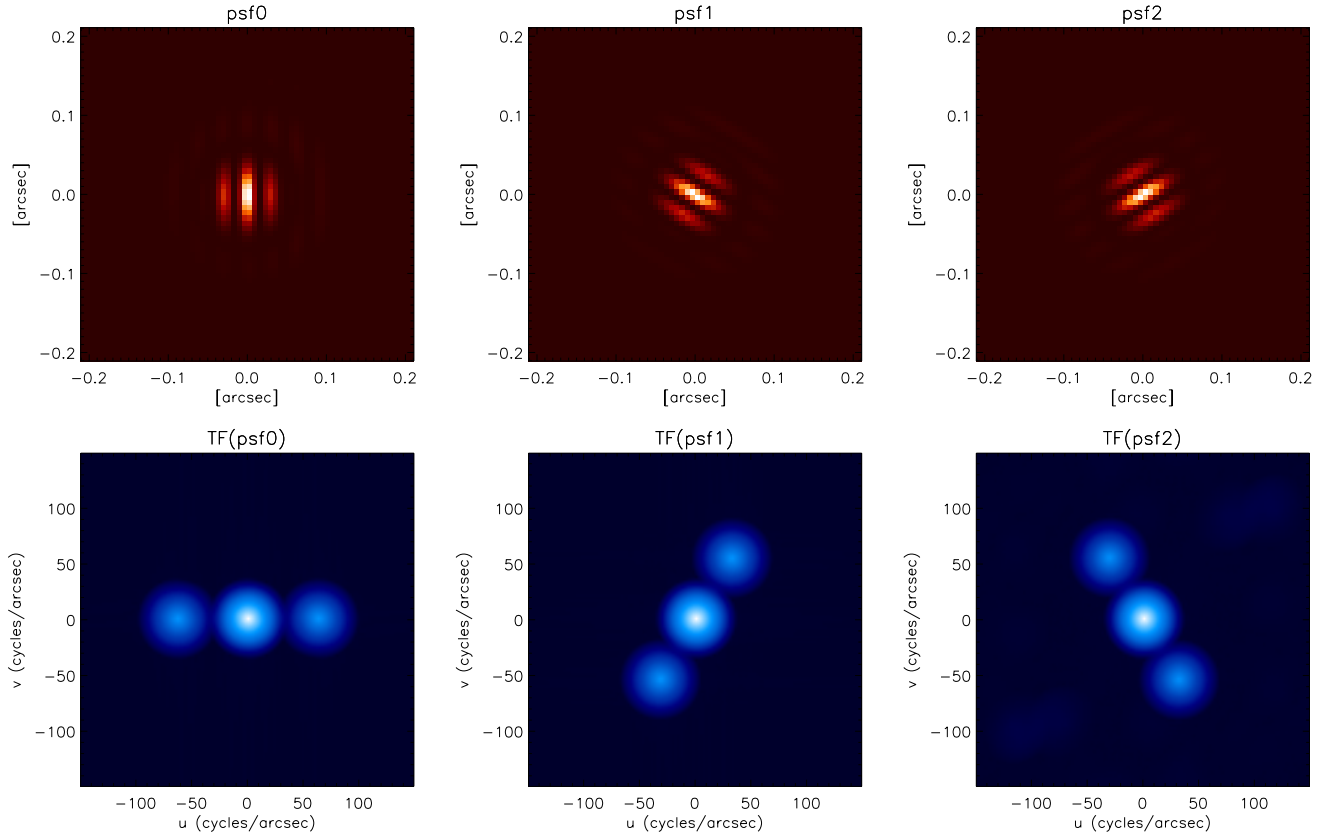


Figure 2. Top: LBT interferometric PSFs at (relative) parallactic angles of 0° , 60° , and 120° . Bottom: corresponding OTFs showing the (instantaneous) u - v coverage.

3. PARTIAL ANGULAR COVERAGE AND ANGULAR SMEARING

The parallactic angle q depends upon the object declination δ and the hour angle H following:

$$q = \arctan \left(\frac{\tan \phi \cos \delta - \sin \delta \cos H}{\sin H} \right),$$

where ϕ is the latitude of the observatory ($+32.667^\circ$ in the case of LBT). The implication is twofold. First: The range of parallactic angles accessible during the night for an object at a given declination can be limited (i.e. less than 180°), implying an incomplete coverage of the u - v plane. Second: Due to the variation of the fringe pattern rotation rate during the night, the variation of parallactic angle during the integration time can induce significant differences in angular range for different baseline orientations, and especially when the object passes close to the zenith.

We report in Table 1 the ranges corresponding to the three relevant cases we have selected: a "wide" case ($\delta=+80^\circ$), a "narrow" case ($\delta=-20^\circ$), and a (close to) "zenith" case ($\delta=+30^\circ$)*. While the "wide" case readily permits a complete coverage of the u - v plane with in addition no problem of angular smearing, the "narrow" case leads to an incomplete angular coverage ($\sim 60^\circ$), and the "zenith" case suffers from a significant variation of the parallactic angle around $H=0$ (up to $\sim 270''/s$). In the last case the concern that naturally rises is about the effect of angular smearing, and hence its comparison with respect to noise increasing if shortest exposures are considered in order to overcome the angular smearing effect.

*note that the reported ranges of parallactic angle q are obtained by considering an airmass < 2

Table 1. Range of hour angle H and corresponding range of parallactic angle q , field rotation velocity \dot{q} , and integration time Δt corresponding to an angular smearing of 5° , in function of the object declination δ , for LBT.

case	δ ($^\circ$)	range H ($^\circ$)	range q ($^\circ$)	\dot{q}_{max} ($''/s$)	\dot{q}_{min} ($''/s$)	Δt_{max} (min)	Δt_{min} (min)
wide	+80	204	216	17.3	14.2	20	16.0
narrow	-20	60	58	15.8	12.3	24	19.0
zenith	+30	142	135	271.0	4.5	72	1.1

We use as astronomical testing object a model of young binary star consisting of a core binary star surrounded by a dusty circumbinary ring. The model is directly inspired by near-infrared observations of the T-Tauri binary star of the quadruple system *GG Tau* and their consecutive data interpretation/modelization.^{17,20} This type of object is challenging for restoration methods: it combines point-like features (the core binary star) and a diffuse one (the circumbinary ring), with a high-dynamic range between them, as it can be seen from Fig. 3 [top]. We chose for the binary a separation of ~ 40 mas (twice the angular resolution of LBT in K-band but still unresolved by a single eye of LBT) and a difference of magnitude of 1. The circumbinary ring is characterized by an integrated K-magnitude of 15.25, with respect to 10 for the main component of the binary star. From the restoration of this object we then compute the error on the parameters of the core binary star (angular separation & position angle, and difference of magnitude Δm). We also evaluate the restoration error of the morphological parameters of the circumbinary ring (radial intensity profile and azimuthal intensity profile), before and after supposing a perfect PSF-subtraction of the core binary (and hence permitting to extrapolate our results to the generic case of extended faint objects). Additional global parameters of our simulations are a total efficiency (mirror+optics+detector) of 25%, a sky background of $12.5 \text{ mag}''^2$ and a read-out noise of $2 e^-$ rms.

Figure 3 shows the difference between the "wide" and "narrow" angular coverage together with the result of the reconstruction on our complete testing object and on the circumbinary ring alone. Exposures of 20 min were considered (six for the "wide" case and three for the "narrow" case, distributed within the available angular range). As it can be seen, the limitation in angular coverage still allows acceptable results. Figure 4 [top] shows the effect of angular smearing in the "zenith" case: the central PSF is integrated over 76° , leading to the clearly noticeable angular smearing. In order to study this effect versus the lack of photons resulting from splitting the smeared images into three angularly equispaced short exposures of 1 min, we have considered the three additional PSFs represented also in Fig. 4 [bottom]. We call this last case the "zenith/5 baselines" case.

The results of the two kind of comparisons are reported in Fig. 5 where the error on the difference of magnitude of the core binary, together with the relative error on the azimuthal profile of the circumbinary ring, are plotted. Our main conclusions are:

- The accuracy in the retrieval of the core binary parameters is definitely better when the coverage is complete ("wide" case), or almost complete without angular smearing ("zenith/5 baselines" case), even though the absolute errors are remarkably small in all cases.
- While the use of short exposure images in order to overcome the problem of angular smearing (from the "zenith" case to the "zenith/5 baselines" case) permits a better precision in the restoration of the core binary parameters, practically at the same level of the "wide" case, this is not true for the circumbinary ring restoration where the expected effect of noise increasing is evident. Hence a trade-off has to be found when dealing with imaging of extended faint objects.

A general remark is that only the high spatial frequencies (i.e. behind the frequency corresponding to the cut-off frequency of the single pupil) are sensible to the incomplete $u-v$ coverage. The natural attenuation of the two interferometric regions of the $u-v$ plane by the OTF makes this limitation more critical for the case of objects with small and faint structures.

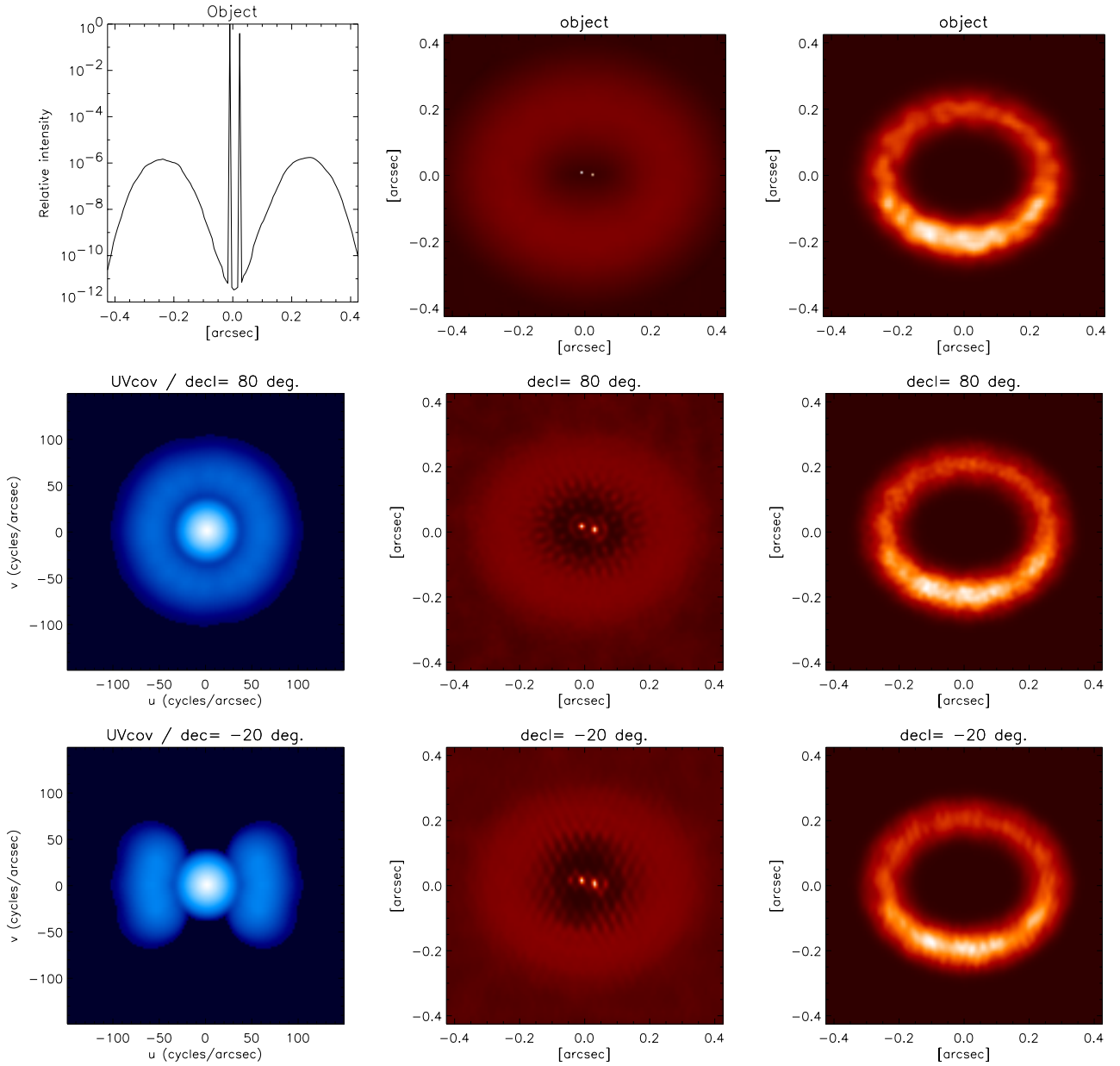


Figure 3. Top: from left to right: log-cut of our *GG Tau*-like modeled object, the whole object, and the circumbinary ring alone. Image rendering is at the power of 0.1. Middle: from left to right: $u-v$ coverage of the "wide" case, corresponding restoration of the whole object, and corresponding restoration of the ring alone. Bottom: from left to right: $u-v$ coverage of the "narrow" case, corresponding restoration of the whole object, and corresponding restoration of the ring alone.

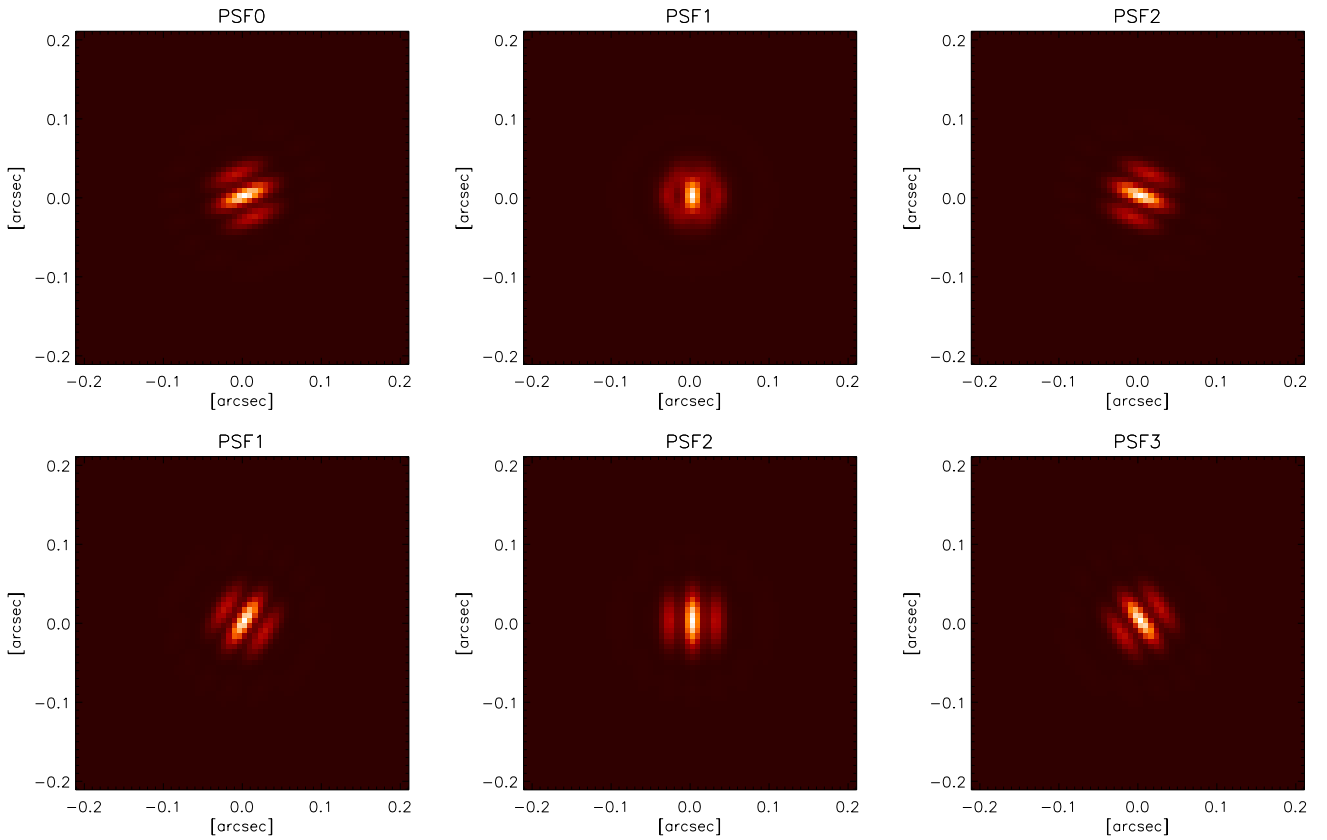


Figure 4. Top: the set of PSFs of the "zenith" case, showing the angular-smeard PSF (middle). Bottom: the three PSFs taken instead of the previous smeard one for the "zenith/5 baselines" case.

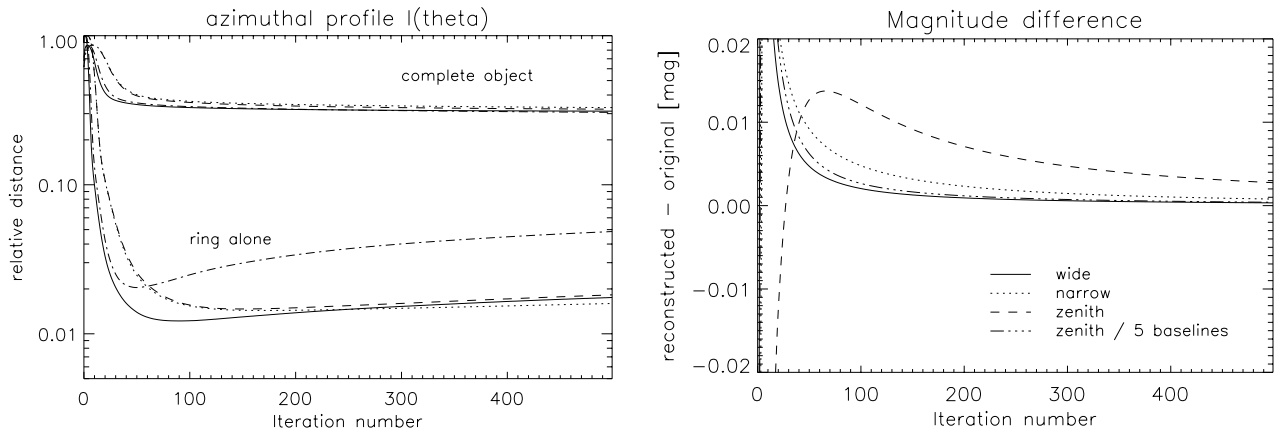


Figure 5. Restoration error plots as a function of the number of OS-EM iterations: in the case of the azimuthal profile of the circumbinary ring [left], and in the case of the difference of magnitude of the core binary [right].

In addition it is interesting to note that the ring curves show a global minimum around 100-200 iterations, whereas the binary curves tend to converge indefinitely. This feature of "semiconvergence"¹ is well-known in the theory of iterative restoration methods and is clearly due to the phenomenon of "noise amplification".¹⁹ We can then conclude that the definition of a reliable stopping-rule^{13,14} would be of great help when dealing with real data.

4. PARTIAL (AND SPACE-VARIANT) ADAPTIVE OPTICS CORRECTION

The effects of partial correction on a single-pupil telescope have the global consequence that the image of a point-source is not exactly an Airy disc, but a central core surrounded by a halo where the first Airy ring is typically broken. In the case of interferometry we have also to consider the differential piston that produces a motion of the fringe pattern along the baseline axis. In a similar way the differential tip-tilt, resulting from the tip-tilt residuals of each single pupil that causes a global motion of the single images, has the effect of a bad superimposing of the two single-pupil envelopes, deforming the interferometric PSF. In the other hand high-orders residuals cause the interferometric PSF to be composed of a central fringed core together with a "speckle-ized" halo where each speckle-like feature is fringed as well.

We are here interested in both the global level of AO-correction and space variance of the AO-corrected PSFs, within the frame of LBT and our OS-EM multiple deconvolution scheme. We therefore consider two case-studies:

1. Starting from the known performance of the first-light AO system of LBT,^{6,9} and assuming that at least the single-conjugate phase of NIRVANA/LINC will have a similar behavior, we define different sets of parameters of our simulation of AO-corrected interferometric PSF leading to different global levels of AO-correction (coming from different magnitudes of the guide star (GS) and subsequent parameters of the system). We therefore assume to be interested in the observation of an object in K-band (sensing wavelength is $\sim R$) at a certain constant angular distance from the GS (here 15"). The resulting set of interferometric reference images (PSF since the reference is supposed to be point-like) and object images are then composed from observations at different parallactic angles (here again 0°, 60°, and 120°), corresponding to three different moments during the observation night, and then to three different realizations of the turbulent atmosphere. The AO system behavior is simulated with the Software Package CAOS.^{4,23} The differential piston is simply attenuated by a certain factor (no real simulation of the correction of it).
2. Assuming observation at a given global level of AO correction, we consider a given object at an increasing angular distance from the reference star. This is equivalent to consider an increasing anisoplanatism error that affects the AO correction. We then rather look at the difference between the reference PSFs and the object PSFs (and the effect on the reconstruction process), than to the global level of AO correction. The different sets of PSFs result this time from taking different angles between the two, i.e. different off-axis angles from the GS, from 0 towards what we can call the "maximum angle of correction" θ_{\max} , which corresponds roughly to half the on-axis Strehl ratio (SR). Resulting median SR of each set are: 94% (on-axis), 93%, 88%, 81%, and 53% (nearly θ_{\max}).

Figure 6 shows the result of one of the simulations of global level of AO-correction runned. The instantaneous wavefront during AO-correction are represented, together with the resulting on-axis reference PSF and binary star image at 15" off-axis.

4.1. Space-variance of the AO-corrected PSF

For this study four sets of LBT interferometric images are generated by convolving our *GG Tau*-like object, used also in previous section, with the four sets of PSFs corresponding to the four SR median values indicated in point 2 of the beginning of this section, and by adding to the result the sky background emission and the different noises. The obtained sets of images are then deconvolved using the corresponding reference PSFs. The results are then again evaluated in terms of retrieval of the core binary parameters, and circumbinary ring

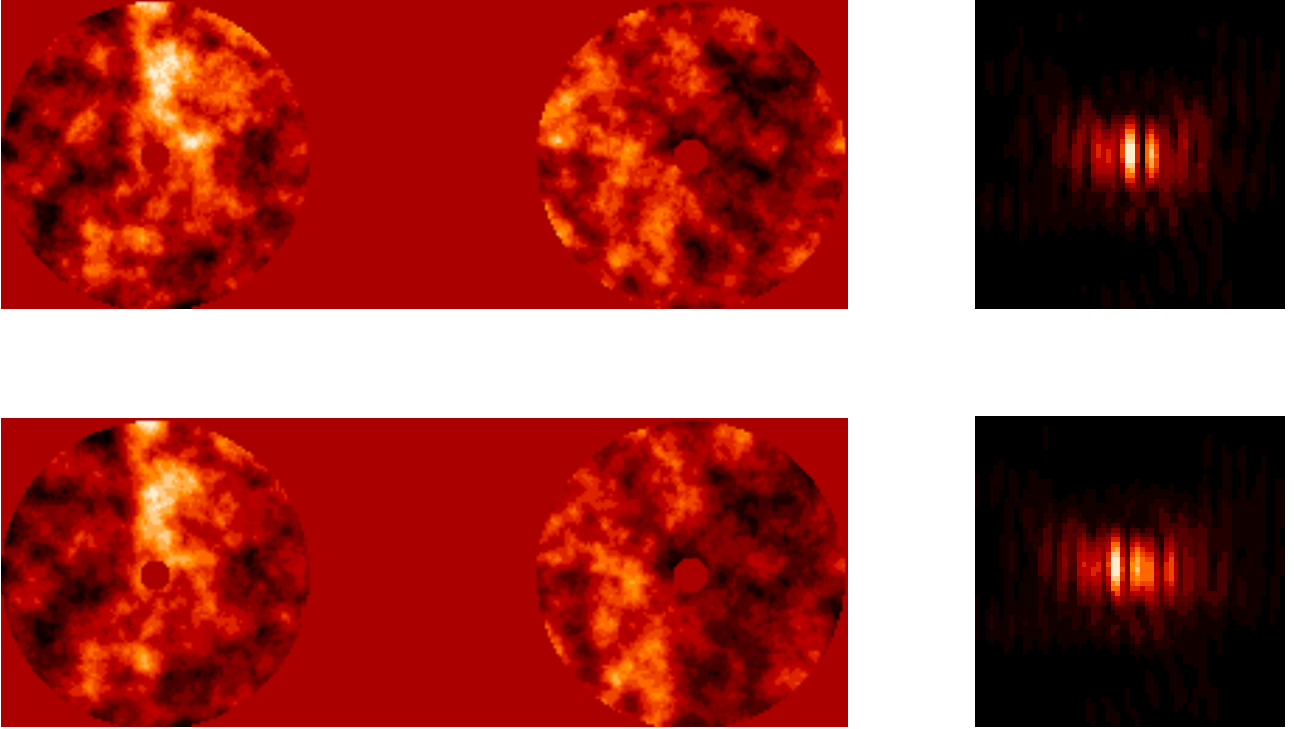


Figure 6. From left to right: wavefront residuals during AO-correction, and corresponding interferometric image: for the on-axis reference star [top], and for the binary star taken in Sec. 4.2 at 15'' off-axis [bottom]. The example taken here is the one for the GS @ $m_R=15.6$ of Table 2.

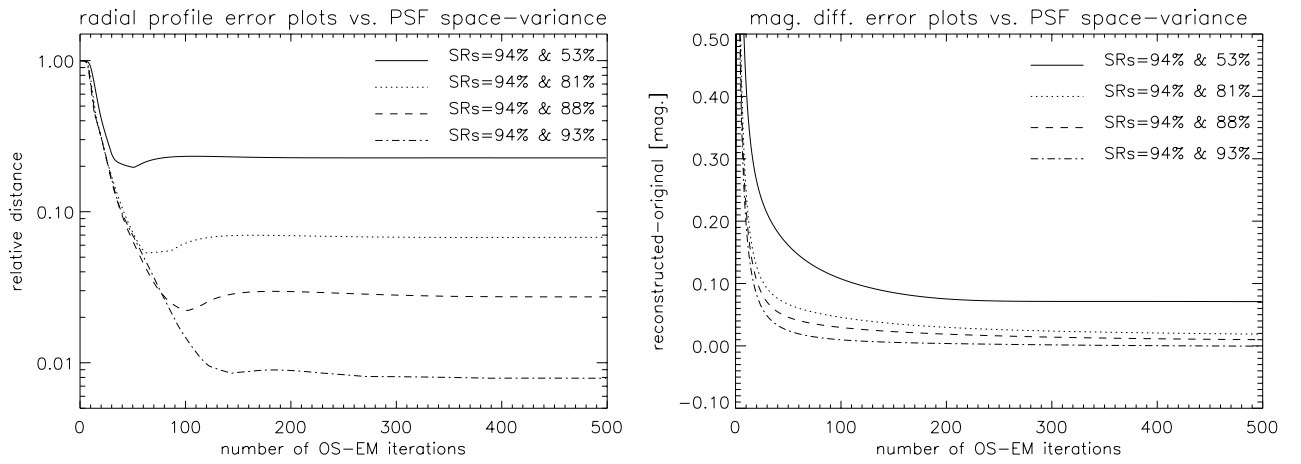


Figure 7. Relative error plots of the radial profile of the circumbinary ring [left], and error plots of the difference of magnitude of the core binary [right], looking at the space-variance of the AO-corrected PSF.

Table 2. R-magnitude of the GS used during AO correction, number of mirror modes corrected, range of additional differential piston residual considered, and resulting K-band SRs obtained.

AO GS R-mag	mirror modes corrected	diff. piston rms [nm]	S_K @ 0° (reference/object)	S_K @ 60° (reference/object)	S_K @ 120° (reference/object)
9.6	496	~ 0	94.7 / 77.1	94.2 / 78.2	94.8 / 73.3
12.6	136	10–20	80.9 / 69.1	78.9 / 66.0	77.6 / 60.2
14.6	66	20–40	56.4 / 48.2	55.3 / 46.8	52.2 / 40.0
15.6	55	50–100	35.8 / 27.2	34.8 / 25.4	35.6 / 25.6
16.6	45	100–200	10.5 / 08.4	18.5 / 14.8	13.6 / 10.6

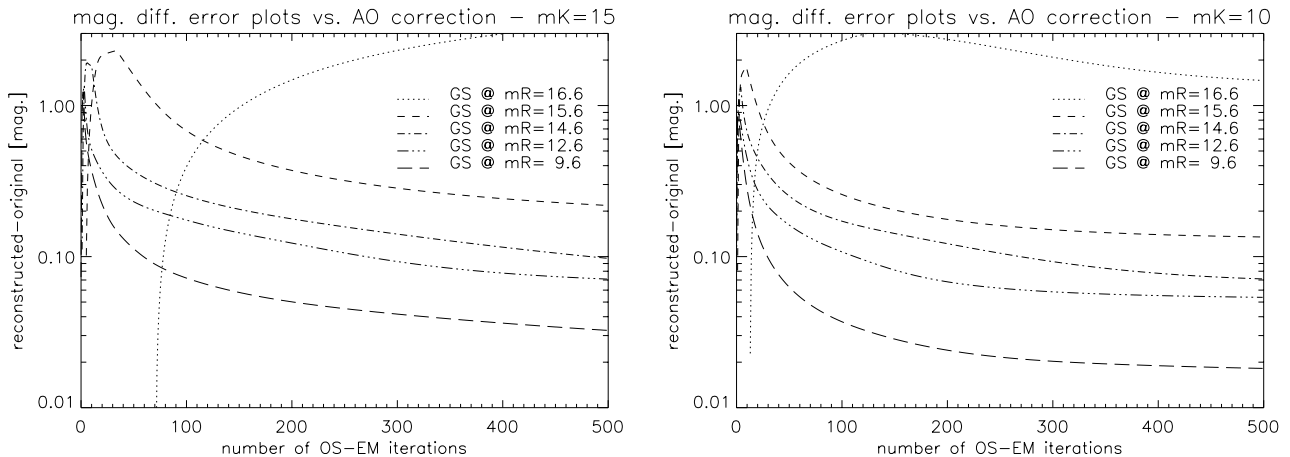


Figure 8. Error plots of the difference of magnitude of a binary star, looking at different global levels of AO correction of the set of interferometric images: [left]: with a main component of K-magnitude 15, [right]: with a main component of K-magnitude 10.

profiles. Figure 7 shows the resulting plots in function of the number of OS-EM iterations, for the difference of magnitude of the core binary star (right), and the radial profile of the circumbinary ring (left).

As expected the closer the reference to the object (and hence the better the PSF estimation), the better the reconstruction. Anyway it has to be noted that in the worst case scenario (SRs=94% & 53%), the error is less than 0.07 mag for the core binary Δm –which is small indeed, and $\sim 20\%$ for the radial profile of the circumbinary ring; with a quick convergence around 100 iterations only in all cases.

4.2. Global AO-correction quality

Table 2 is a résumé of the parameters and SRs obtained for each simulated situation of global level of AO-correction. The AO GS R-magnitude is reported together with the number of LBT 672 adaptive secondary mirror modes corrected, the additional differential piston rms (no real simulation of its adaptive correction), and the resulting SR in K-band for each set and each parallactic angle.

Five sets of reference PSFs are so considered together with five sets of images of an astronomical object of interest. In this section we consider two of them: first a binary star of main component K-magnitude 15, difference of magnitude 1, and angular separation ~ 45 mas; and second a *Butterfly Star*-like object which is, with respect to IRAS 04303+2247 (a bipolar nebulae seen in scattering light —called *the Butterfly Star in Taurus* by Lucas & Roche¹⁵ and imaged with HST by Padgett et al.¹⁶), put at 1.4 Kpc instead of 140 pc, and with an integrated K-magnitude of 14.

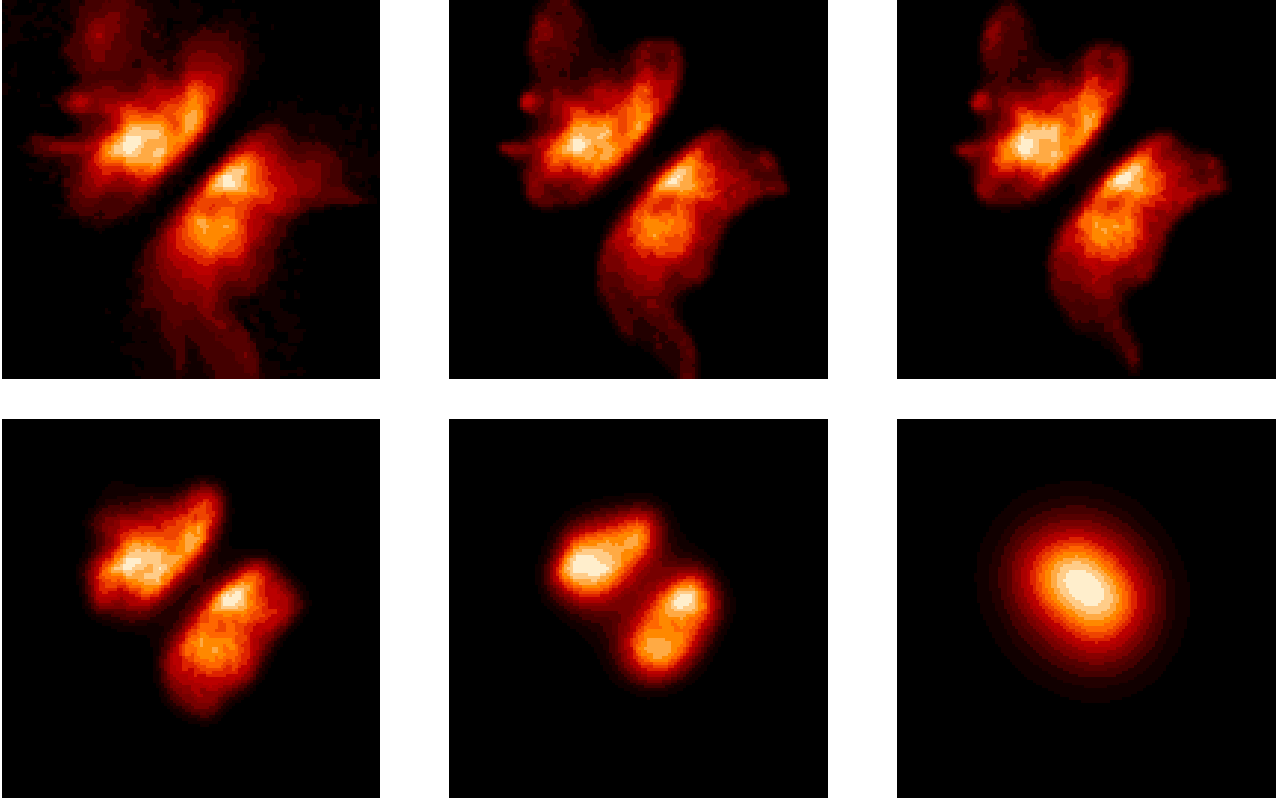


Figure 9. Reconstruction of the *Butterfly Star*-like object for different global AO quality. From left to right and from top to bottom: the object, the results of the reconstruction with decreasing global AO-correction quality following Table 2.

The results concerning the restoration of the binary star are reported in Fig. 8 [left]. While the error on the restoration of the difference of magnitude goes from ~ 0.03 mag to ~ 0.2 mag when going from the best case (GS @ $m_R=9.6$) to the case “GS @ $m_R=15.6$ ”, the worst-case scenario (GS @ $m_R=16.6$) is clearly not converging towards a reasonable solution: the PSF estimation is too bad in the last case ($\langle SR \rangle \sim 13\%$). The right-part of Fig. 8 shows the result of the same simulation but with a main component of K-magnitude 10: this is directly comparable with the previous results on the *GG Tau*-like object. We note that the result for GS @ $m_R=9.6$, which is very similar to the case “SRs=94% & 81%” of previous subsection, leads to exactly the same precision on the difference of magnitude (~ 0.02 mag). The results show once again how a major difference in the PSFs, this time mainly due to an increasing number of modes from the atmosphere that remain uncorrected (rather than to an increasing pure anisoplanatism error), and then a poorer estimation of the PSF corresponding to the image formation relation of the observed object, leads to a decreasing precision of the reconstruction, and even in a wrong one (see the worst case: “GS @ $m_R=16.6$ ”).

Figure 9 shows the reconstructions obtained with the same sets of AO-corrected PSFs but with our *Butterfly Star*-like object. The effect of decreasing global AO-correction quality is here again evident: while the best case leads to an almost perfect reconstruction, the high-frequency features are more and more badly reconstructed with, in the worst case, the bipolar feature that is not even recognisable.

The fact that the quality of the restoration degrades with decreasing SR values can be understood in terms of signal-to-noise ratio (SNR) in the Fourier space. Indeed this degradation is a consequence of the lower SNR of the high spatial frequencies which are more attenuated for the OTF corresponding to lower SR. The compensation of the OTF provided by the restoration being independent of the SNR of the high spatial frequencies, hence the degradation.

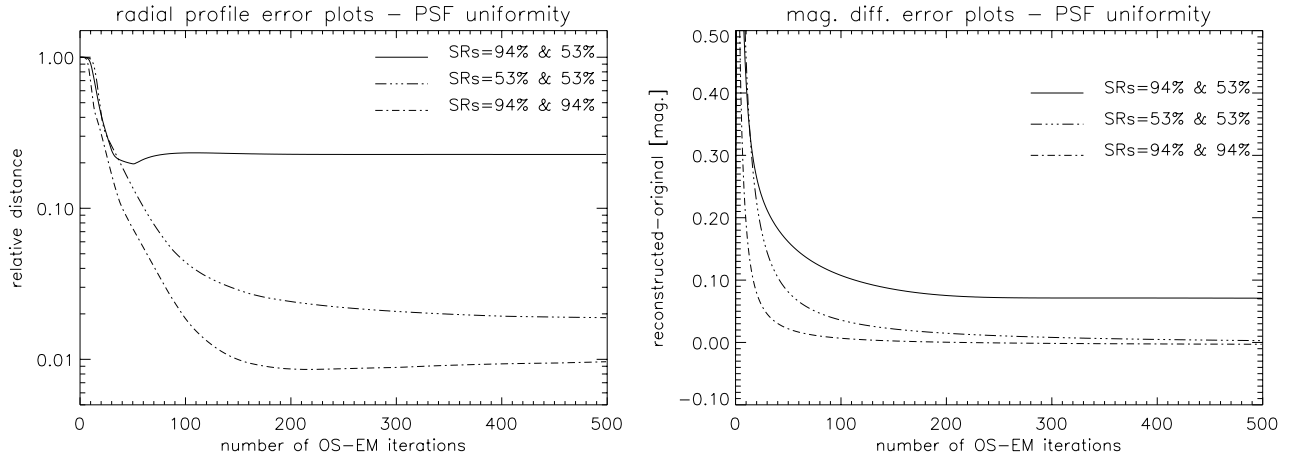


Figure 10. Relative error plots of the radial profile of the circumbinary ring [left], and error plots of the difference of magnitude of the core binary [right], considering a uniform-PSF MCAO system.

5. DISCUSSION

For what concerns the adopted method, OS-EM, we have found that it is a convenient tool for at least a quick look of the observations with LBT, even in the case of high-dynamic range imaging (cf. the tests performed on our modeled *GG Tau*-like object).

The angular coverage and smearing seems, at the light of the simulations performed, not to affect significantly the large structure of the image nor the parameters of the binary, but only the convergence rate of the iterative method. Having being faced anyway with the problem of noise amplification when dealing with faint extended objects, we are currently studying the possibility of implementing criteria for stopping the iterations or for choosing regularization parameters. Another possible prospect concerns the improvement of the PSF estimates directly in the restoration process. This is the case of the so-called myopic or blind deconvolution algorithms which make use of some additional physical constraints in order to estimate simultaneously the object and the PSFs sets,^{11,12} breaking the degeneracy of the problem. These methods can also be useful for the problem of space-variant PSFs, although on a FoV where the PSFs can be still considered as non-variant (to fulfill the convolution relation of image formation).

About PSF uniformity, Fig. 10 shows the comparison between the restoration of the core binary star of our *GG Tau*-like object for the case of non-uniform PSFs ("SRs=94% & 53%" case), and for perfectly uniform PSFs at two different regimes of AO-correction: the "SRs=53% & 53%" case, and the SRs=94% & 94%" case. It is clear from these plots that uniformity is a main issue for this observational technique, even at the cost of a lower average SR, at least for the field of application we have considered. Such a condition, which may be satisfied by an MCAO system like NIRVANA/LINC for LBT, is also required by the model of image formation assumed in the deconvolution method and implies that the PSF obtained from a reference star provides a good approximation of the PSF which must be used in the process of image restoration. From the point-of-view of the system design and strategy of AO-correction/observation this is also an interesting information. For example in V erinaud et al.²⁴ it is shown that, in the framework of the layer-oriented MCAO technique, the multiple-FoV scheme insure a better uniformity of the SR across the corrected FoV, at the cost of a slightly lower global SR. By cross-checking with the results of the present paper, we can conclude that this would be the best way of observing in wide-field interferometric imaging mode with LBT. While this conclusion holds with no doubt for $SR \gtrsim 50\%$, the physics of the residuals in the halo could lead to different conclusions in cases of low-SR *and* MCAO, where other factors like the geometry of the asterism of GS' could play a certain role. In order to verify this we plan to do a complete study of it, including also a more realistic simulation of the correction of differential piston.

ACKNOWLEDGMENTS

All the work presented in this paper was done with the help of the Software Package AIRY, version 1.0, and the Software Package CAOS, version 3.6. The Software Package AIRY is obtainable under request and subscription to its dedicated mailing-list by visiting the web site <http://dirac.disi.unige.it>. The Software Package CAOS is obtainable under request and subscription to its dedicated mailing-list by visiting the web site <http://www.arcetri.astro.it/caos>. Both software packages are delivered together with the CAOS Application Builder (version 3.1): the IDL-based graphical environment within which they were developed.

We thank Piero Ranfagni for his help in astrometry, Piero Salinari, Armando Riccardi, and Roberto Ragazzoni for useful discussions, Luca Fini for the graphical programming environment associated with AIRY and CAOS, and Christophe Vérinaud for both the development of tools within CAOS that permitted the new simulations presented within this paper and many fruitful discussions.

REFERENCES

1. M. Bertero & P. Boccacci, *Introduction to Inverse Problems in Imaging*, IOP Publishing, Bristol 1998.
2. M. Bertero & P. Boccacci, *Astron. Astrophys. Suppl. Ser.* **144**, pp. 181, 2000a.
3. M. Bertero & P. Boccacci, *Astron. Astrophys. Suppl. Ser.* **147**, pp. 323, 2000b.
4. M. Carillet, L. Fini, B. Femenía, A. Riccardi, S. Esposito, É. Viard, F. Delplancke, N. Hubin, in *ASP Conf. Series* **238**, F. A. Primini & F. R. Harnden Eds, pp. 249–252, 2001.
5. M. Carillet, S. Correia, P. Boccacci, M. Bertero, *Astron. Astrophys.* **387**, pp. 744–757, 2002a.
6. M. Carillet, C. Vérinaud, S. Esposito, A. Riccardi, B. Femenía, A. Puglisi, Proc. SPIE 4839, P. L. Winizowitch & D. Bonaccini Eds, to be published, 2002b.
7. S. Correia, M. Carillet, L. Fini, P. Boccacci, M. Bertero, A. Vallenari, A. Richichi, M. Barbati, in *ASP Conf. Series* **238**, F. A. Primini & F. R. Harnden Eds, pp. 404–407, 2001.
8. S. Correia, M. Carillet, P. Boccacci, M. Bertero, L. Fini, *Astron. Astrophys.* **387**, pp. 733–743, 2002.
9. S. Esposito, A. Tozzi, D. Feruzzi, M. Carillet, A. Riccardi, L. Fini, C. Vérinaud, M. Accardo, G. Brusa, D. Gallieni, R. Biasi, C. Baffa, V. Biliotti, I. Foppiani, A. Puglisi, R. Ragazzoni, P. Ranfagni, P. Stefanini, P. Salinari, W. Seifert, J. Storm, Proc. SPIE 4839, P. L. Winizowitch & D. Bonaccini Eds, to be published, 2002.
10. L. Fini, M. Carillet, A. Riccardi, in *ASP Conf. Series* **238**, F. A. Primini & F. R. Harnden Eds, pp. 253–256, 2001.
11. T. Fusco, J. P. Véran, J. M. Conan, L. M. Mugnier, *Astron. Astrophys. Suppl. Series* **134**, pp. 193, 1999
12. S. M. Jefferies & J. C. Christou, *ApJ* **415**, pp. 862, 1993
13. H. Lanteri, R. Soummer, C. Aime, *Astron. Astrophys. Suppl. Series* **140**, pp. 235, 1999a.
14. H. Lanteri, M. Roche, O. Cuevas, C. Aime, Proc. SPIE **3866**, A. Kohle & J. D. Gonglewski Eds, pp. 144, 1999b.
15. P. W. Lucas & P. F. Roche, *MNRAS* **286**, pp. 895, 1997.
16. D. L. Padgett, W. Brandner, K. R. Stapelfeldt, et al. *AJ* **117**, pp. 1490, 1999.
17. C. Roddier, F. Roddier, M. J. Northcott, J. E. Graves, K. Jim, *ApJ* **463**, pp. 326, 1996.
18. L. A. Shepp & Y. Vardi *IEEE Trans. Med. Imaging* **MI-1**, pp. 113, 1982.
19. R. L. White, in *The Restoration of HST Images and Spectra II. Space Telescope Science Institute*, Hanish R. J. & White R. L. Eds, pp. 104, 1994.
20. K. Wood, M. Crosas, A. Ghez, *ApJ* **516**, pp. 335, 1999.
21. R. Ragazzoni, T. Herbst, D. Andersen, P. Bizenberger, H.-W. Rix, R.-R. Rohloff, C. Arcidiacono, E. Diolaiti, S. Esposito, J. Farinato, A. Riccardi, É. Vernet-Viard, P. Salinari, Proc. SPIE 4839, P. L. Winizowitch & D. Bonaccini Eds, to be published, 2002.
22. A. Riccardi, G. Brusa, P. Salinari, D. Gallieni, R. Biasi, M. Andrighettoni, H. M. Martin, Proc. SPIE 4839, P. L. Winizowitch & D. Bonaccini Eds, to be published, 2002.
23. C. Vérinaud, M. Carillet, B. Femenía, in *Semaine de l’Astrophysique française*, Paris, June 2002.
24. C. Vérinaud, C. Arcidiacono, M. Carillet, E. Diolaiti, É. Vernet-Viard, R. Ragazzoni, S. Esposito, Proc. SPIE 4839, P. L. Winizowitch & D. Bonaccini Eds, to be published, 2002.